Kinematics of cluster-forming hub-filament systems

Author: Marta Morera Lizano
Facultat de Física, Universitat de Barcelona, Diagonal 645, 08028 Barcelona, Spain.

Advisor: Gemma Busquet Rico

Abstract: We present ALMA observations of the molecular line transition $C^{18}O\,(1–0)$ in the north region of the molecular cloud G14.225-0.506. We aim to demonstrate the existence of filamentary structures that channel the flow of gas towards the embedded stellar cluster. We found that the spectral profile of the region has two main velocity components, the more intense and therefore dominant one is around ~ 20 km s^{-1}, and it is associated with the cloud. We identified 20 relevant structures within the molecular cloud all of them dominated by non-thermal motions indicative of the presence of turbulence, rotation and/or accretion. We selected five structures near to the stellar cluster and studied their kinematics. The results show an accretion of gas towards the cluster and two distinct regions with blueshift (north) and redshift (south).

I. INTRODUCTION

The formation of stellar clusters occurs within molecular clouds, which contain thousands of solar masses of cold gas and dust material. These clouds exhibit a high degree of inhomogeneity, they are shaped in filamentary structures with complex associations between them. They frequently converge towards high-density regions, called hubs (or hub-filament structures, HFS), harboring deeply embedded star clusters [1]. It should be noted that the term "hub" is used to describe a central body of low aspect ratio and high column density, while "filament" is used to refer to an associated feature of greater aspect ratio and lower column density.

A number of filaments of parsec length extend radially from the dense star-forming hubs that have a column density exceeding 10^{22} cm^{-2} [1]. These filaments were previously considered idealised, with the assumption that they behaved in accordance with the hydrostatic equilibrium equation and quasi-static gravitational fragmentation. However, over time, it has become evident that this is an oversimplification. Filaments have been observed to behave in a manner that is more complex than previously assumed. The study of these structures now considers magnetic fields, external pressure and the non-isolation of filaments to play an important role, as do the lack of resemblance to static structures [2]. When all non-idealised aspects are taken into account, the emplacement of these filaments tends to be in an orientation that is nearly parallel to one another and directed along the short axis of the hub. When the magnetic field is taken into account, elongated structures of low density appear near the molecular cloud, called striations, which are perpendicular to the filaments [2]. The disposition and geometry of filaments and hubs indicate that filaments act as rivers, channelling flows of gas nurturing the embedded stellar cluster [3].

This work focus on the northern region of the G14.225-0.506 molecular cloud (hereafter G14.2-North). The distance to these cloud is estimated to be $1.6^{+0.3}_{-0.1}$ kpc [4], obtained from *Gaia* DR2 parallax measurements [5]. G14.2-North consist of a hub-filament system with various filaments in direction north-south that appear, projected in the plane of the sky, parallels between them. The hub contains a deeply embedded stellar cluster with various Young Stellar Objects (YSOs) detected at cm, mm and IR wavelengths [6–8] (see FIG. 1-right).

The goal of this project is to analyse the kinematics of the structures found around the cluster using the molecular tracer $C^{18}O$. The objective is to investigate the velocity gradient and velocity dispersion of the structures.

II. METHODOLOGY

The data analysed in this work was obtained with the Atacama Large Millimeter/submillimeter Array (ALMA [9]; proposal code 2018.1.01347.S, PI: G. Busquet). ALMA is the largest mm/submmillimeter telescope in the world, situated in the Atacama Desert (Chile). It is composed of 66 high-precision antennas, which operate on wavelengths from 0.32 to 7 mm. The observations were conducted using a mosaic of 139 pointings, with the objective of mapping a set of molecular lines at 3 mm across the molecular cloud G14.2. We focus on the study of the $C^{18}O\,(1–0)$ transition (ν = 109.7821734 GHz, taken from The Cologne Database for Molecular Spectroscopy (CDMS; [10])), obtained with the most compact C43-1 configuration (synthesized beam $\sim 3''$).

The observations utilised the ALMA main array and the Atacama Compact Array (ACA). The main array, comprises fifty 12-meter diameter antennas arranged in a specific configuration with distances between 150 m and 16 km. This display simulates a giant telescope that is much larger than any single antenna. Furthermore, ACA is composed of twelve 7-meter antennas with a fixed configuration. It is designed to enhance wide-field imaging, structures larger than about $0.6\times(\lambda/b_{min})$, where b_{min} is the shortest baseline in the interferometer, are not well reproduced in reconstructed images.

Molecular lines are used to analyse the kinematics of

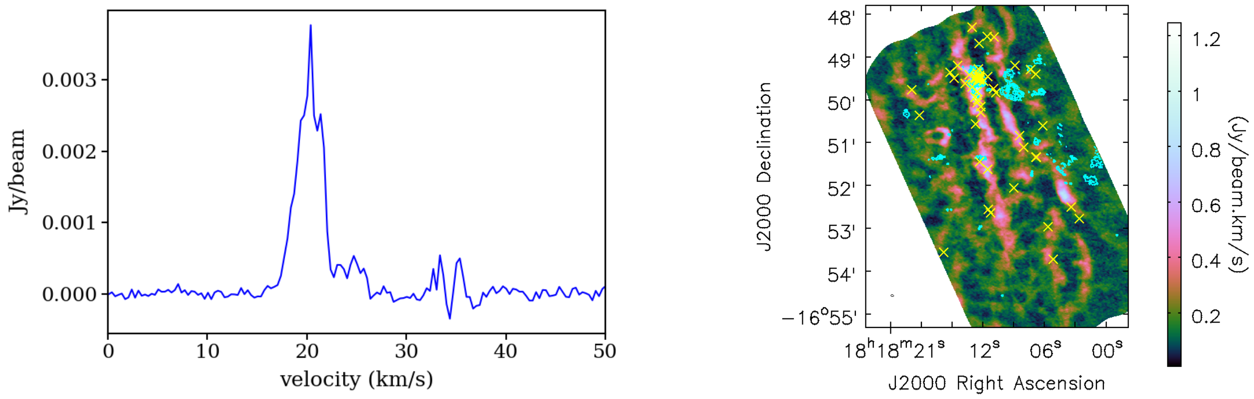

FIG. 1: *Left:* Spectral profile of the C^{18}O (1–0) line over G14.2-North, which shows the intensity in Jy beam^{-1} for each velocity. *Right:* Moment 0 map (integrated intensity) for the velocities 13.39-30.04 km s^{-1} (color scale) and 30.04-38.37 km s^{-1} (cyan contours). Yellow crosses indicate the location of Young Stellar Objects (YSOs) within the region (tabulated in [6–8]).

the gas. The choice of a specific molecule depends on the specific research question being addressed. For instance, for denser filaments, the most commonly employed molecular tracers are NH_3 [11] and N_2H^+ [3]. To study the gas kinematics of filaments and low-density material ($n \simeq 10^3$ cm^3) surrounding denser filaments the molecular tracer used is C^{18}O [12]. Another reason for the use of this molecule is that it is the second most abundant molecule in the Universe, following H_2.

A. C^{18}O (1–0) emission

We employed the Common Astronomy Software Applications (CASA; [13]) to visualise the C^{18}O (1–0) data cube and obtain the spectrum over the entire field of view (see FIG. 1-left). It is evident that the emission is quite complex, displaying different peaks at varying velocities. Nevertheless, we can identify two distinct and clearly separated velocity components. The first one, which is also the strongest component (i.e., main velocity component), corresponding to velocities of approximately 15 to 30 km s^{-1}, in which there is the systemic velocity of the cloud $\sim$ 20 km s^{-1} [11]. The second component (i.e., secondary velocity component) encompasses velocities from 30 to 38 km s^{-1}.

For each of these two velocity components, we present in FIG. 1-right the moment 0 map, which corresponds to the integrated value of the spectrum. The morphology of the C^{18}O (1–0) emission is clearly extended and consists of several filamentary structures elongated in the north-south direction, which appear approximately parallel one to another. Most of the known YSOs in G14.2-North, indicated with yellow crosses, are associated with the hub-filament structure, being more clustered towards the hub region. The secondary velocity component (displayed in contours in FIG. 1-right) is more compact. In the present work, we focus the study of the gas kinematics on the main velocity component.

B. Dendrograms

In order to analyse the complex morphology and hierarchical structure of the C^{18}O (1–0) emission, we used the Dendrogram algorithm [14] through the `astrodendro` package [15]. These diagrams illustrate the relations and hierarchy of structures within the data set. The dendrograms represent the data in a tree form, with a trunk, or base structure, which splits into branches; these branches, in turn, split into smaller sub-structures, called leaves, which do not themselves have further subdivisions. In order to compute the dendrogram, three variables must be specified. The parameter `min_value` corresponds to the minimum value to be considered in the data set, its function is to exclude noise from the dataset. The parameter `min_delta` corresponds to the significance of a leaf, its purpose is to avoid including local maxima that are merely a result of noise. Finally, the minimum number of pixels required for a leaf to be considered an independent entity, denoted by `min_npix`, must be specified; if the leaf has fewer pixels than the value set, it will be combined with a branch or another leaf.

In order to conduct our analysis, we initially explored a range of values for the variables: `min_value` $= 3\sigma, 5\sigma, 6\sigma, 7\sigma$; `min_delta` $= \sigma, 2\sigma, 3\sigma$; and `min_npix` = 6, 12, 24; where σ represents the noise level in the observation, which is $\sigma = 1.6 \times 10^{-2}$ Jy beam^{-1}. A total of 36 dendrograms were computed and inspected, with the one used for analysis being the one with variable values `min_value` $= 3\sigma$, `min_delta` $= 3\sigma$ and `min_npix` = 24. The values of the two final variables were selected because the dendrograms' branches and leaves were simpler, with fewer substructures, which would facilitate the further analysis. The value of `min_value` was chosen as the lowest to exclude noise. In this instance, it can be observed that a greater number of structures originate from the same trunk, whereas in the other cases, they were considered to be individual. Another reason for the selection of the

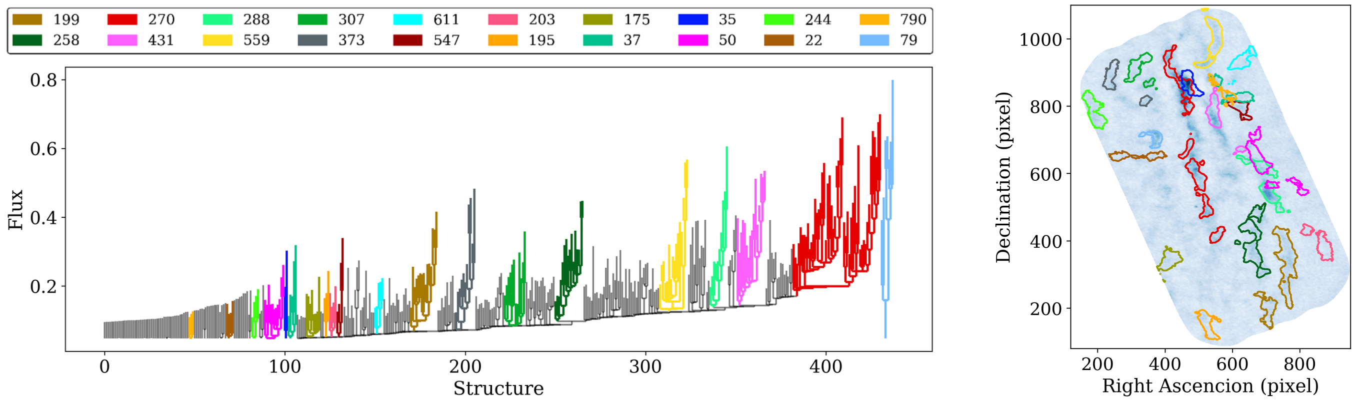

FIG. 2: *Left:* Dendrogram of the region G14.2-North with the variables: `min_value`= 3σ, `min_delta`= 3σ, `min_npix`= 24. The branches of the 20 most relevant structures are highlighted by distinct colors. *Right:* Representation of the contour of the same 20 coloured structures in the dendrogram, overlaid on the moment 0 map.

values of our variables was that the identification of 2939 structures was achieved with the chosen variables (3σ, 1σ, 6), whereas only 797 structures were identified with the variables selected for this study. This approach facilitated the investigation of the general kinematics of the structures and also demonstrated the complexity of the data set and analysis.

III. RESULTS AND DISCUSSION

A. Catalog

FIG. 2 illustrates the dendrogram tree, which includes the most relevant structures that have been selected to proceed with our study. The criteria followed to chose these structures was that their dendrogram must have some level of complexity, allowing for the study of the movements of the substructures, and additionally, they must have a reasonable size in the map. Ultimately, a total of 20 structures were selected which are highligthed in colors in FIG. 2.

Computing the catalog of the structures with `astrodendro` we can obtain their physical properties, including dimensions, velocity and velocity dispersion. In the majority of the structures the longitude is ~ 3 times the width, therefore, they are clearly elongated (see FIG. 2-right). The velocity range can be divided in two groups, velocities around 18.8-21.4 $\mathrm{km\,s^{-1}}$ and 33.1-36.8 $\mathrm{km\,s^{-1}}$, which correspond to the two velocity components identified in the $C^{18}O$ spectrum (see FIG. 1-left). Another parameter provided was the velocity dispersion. The majority of structures present a velocity dispersion between 0.3 $\mathrm{km\,s^{-1}}$ to 0.7 $\mathrm{km\,s^{-1}}$, regardless of their size or location. However, there was one exception, structure 175 has a velocity dispersion exceeding 1 $\mathrm{km\,s^{-1}}$, which may be attributed to the distinguishable two parts that may have different velocities.

From the observations, the total velocity dispersion can be obtained, this is composed of two main components: thermal and non-thermal. We estimated the thermal contribution to determine the significance of non-thermal motions, which can be attributed to turbulence or systematic movements, such as rotation, contraction or expansion. The thermal velocity dispersion was calculated using the following expression:

$$\sigma_{\mathrm{1D,th}} = \sqrt{\frac{k_B\,T}{\mu\,m_{\mathrm{H}}}}, \tag{1}$$

with k_B as the Boltzmann constant, $T \approx 10$ K [11] is the gas kinetic temperature of the molecular cloud, $\mu = 30$ for the molecule weight of $C^{18}O$ and m_{H} the mass of the Hydrogen atom. We obtained $\sigma_{\mathrm{1D,th}} = 0.052\ \mathrm{km\,s^{-1}}$. For the observed velocity dispersion of the entire cloud, with the largest structure in the dendrogram, 92, the value obtained from the Catalog was $\sigma_{\mathrm{1D,obs}} = 0.996\ \mathrm{km\,s^{-1}}$. At this point, it is possible to compute the non-thermal contribution using

$$\sigma_{\mathrm{1D,nth}} = \sqrt{\sigma^2_{\mathrm{1D,obs}} - \sigma^2_{\mathrm{1D,th}}}, \tag{2}$$

which we obtained $\sigma_{\mathrm{1D,nth}} = 0.995\ \mathrm{km\,s^{-1}}$. It can be seen that $\sigma_{\mathrm{1D,nth}} >> \sigma_{\mathrm{1D,th}}$, this means that the non-thermal component has a very important contribution in the molecular cloud behaviour. This means that the main factors for the movement of the filaments are not thermal, but rather turbulence, rotation and/or accretion.

B. Kinematics of the structures

Up until this point, we have discussed the velocity and the velocity dispersion of the different structures. In this section we will examine the direction of the structures' movements. In order to proceed, we analysed each structure separately, using the corresponding dendrogram we selected the larger branches and leaves (the figures for each of the 20 structures are in Appendix V). The same methodology as before can be employed to obtain the velocities of these substructures, these correspond to the velocities in the line of sight. Consequently, the observed redshift or blueshift velocities can be attributed to the substructure's movement away or towards the observer, respectively. The velocity of the entire cloud, which is approximately 20 $\mathrm{km\,s^{-1}}$, determined the threshold value between blueshift and redshift velocities.

FIG. 3 illustrates the case for the structure 270, which shows that the emission in the southern region is redshifted, the structures are moving further away, and in the northern region there is a blueshift, with the structures moving towards us. The transition between redshift and blueshift occurs around the hub. In addition, there is a velocity gradient towards the cluster; the northern part moves downwards, while the southern part moves upwards. Moreover, the substructures in closer proximity to the protocluster exhibit a greater velocity dispersion than those situated at a greater distance.

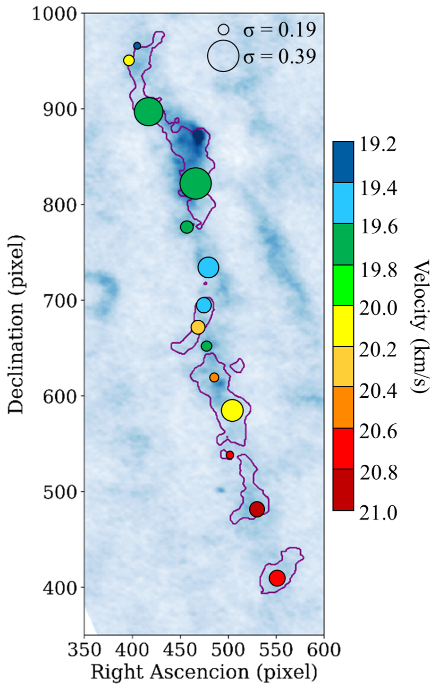

FIG. 3: Velocity and velocity dispersion of the various substructures of the structure 270 highlighted in FIG. 2. The contour in purple corresponds to substructure 270 and is overlaid with the moment 0 in a blue scale. The circles represent each substructure, with the colour of the symbols indicating the gas velocity and the size denoting the velocity dispersion. It should be noted that the dark blue circle at the top has a velocity dispersion of 0, but it was included to represent its velocity.

Considering the structures from the main velocity component that are in the vicinity of the cluster (307, 270, 559, 431 and 790), with the same methodology as previously stated, we determined their gas kinematics. FIG. 4 illustrates that two very distinct regions can be identified, with the northern region exhibiting a blueshift and the southern region exhibiting a redshift. Furthermore, it can be observed the manner that filaments facilitate the flow of gas towards the protocluster or other filaments that extend to the cluster. This suggests a large-scale global collapse towards the cluster.

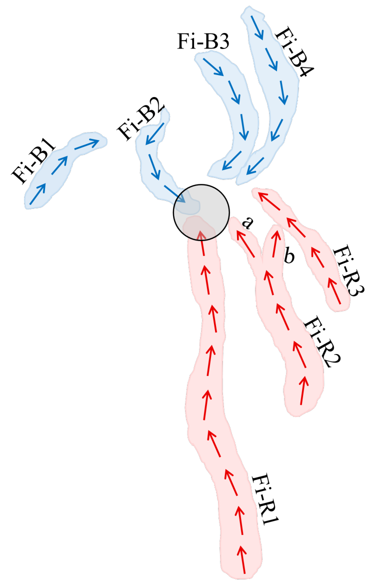

FIG. 4: Schematic representation of the structures 307, 270, 559, 431 and 790 of the molecular cloud G14.2-North velocity field (arrows) viewed on the plane of the sky. The colours red and blue are used to indicate a redshift or blueshift, respectively. The hub is indicated by the black and grey circle.

TABLE I: Values of the longitude and velocity gradient of the filaments indicated in FIG. 4 with the ID of the structure they correspond.

Filament	Structure	Longitude (pc)	∇V (km s^{-1} pc^{-1})
Fi-B1	307	0.981	0.203
Fi-B2	270	1.189	0.218
Fi-B3	559	1.977	0.578
Fi-B4	559	2.692	0.163
Fi-R1	270	5.998	0.188
Fi-R2a	431	2.925	0.683
Fi-R2b	431	2.938	0.476
Fi-R3	790	1.988	0.494

To study the movements in the line of sight qualitatively, we computed the velocity gradient of the selected filaments. In order to determine the length of the structures with the greatest possible accuracy, we calculated the distance between the centres of two adjacent substructures (values of the centre position obtained from the Catalog) and for the substructures in the corners we added half of their longitude. This method was employed in preference to the sum of the longitudes of each substructure or the distance between the first and last substructure, as the filaments are not straight lines (see

FIG. 2-right) and the substructures may overlap or be a part. Using the velocities of the substructures in the corners we obtained the velocity gradients presented in TABLE I. The range of the velocity gradients is from 0.16 to 0.68 $\mathrm{km\,s^{-1}}$, with no discernible pattern evident regarding size, location or redshift/blueshift.

IV. CONCLUSIONS

In this work, we present the results obtained from the molecular transition $C^{18}O$ (1–0) observations carried out with ALMA in the northern region of molecular cloud G14.2. We studied the kinematics of filaments, with the velocity, dispersion velocity and velocity gradient around the protocluster of YSOs. The results of our study lead to the following conclusions:

1. The molecular cloud exhibits two distinct velocity ranges. The main velocity component is 15-30 $\mathrm{km\,s^{-1}}$, which displays filamentary structure in the north-south direction in parallel alignment. The secondary velocity component, which ranges between 30-38 $\mathrm{km\,s^{-1}}$, is more compact in form.

2. A total of 20 relevant structures were identified, with the majority presenting an elongated geometry, velocities of 18.8 to 36.8 $\mathrm{km\,s^{-1}}$ and velocity dispersion 0.3 to 1.1 $\mathrm{km\,s^{-1}}$.

3. The non-thermal contribution of the velocity dispersion, $\sigma_{\mathrm{1D,nth}} = 0.995\ \mathrm{km\,s^{-1}}$, is considerably larger than the thermal component, $\sigma_{\mathrm{1D,th}} = 0.052\ \mathrm{km\,s^{-1}}$. This is an indicative of the significance of non-thermal motions such as turbulence or other systemic motions like rotation and/or accretion.

4. Eight filaments have been identified in the vicinity of the embedded stellar cluster. These filaments contribute to the accretion of gas towards the cluster or accretion to a larger filament, which has a direct flow of gas towards the cluster.

5. G14.2-North exhibits a large-scale global collapse and an inflow of gas, driven by filaments, towards the protocluster.

Further analysis of additional filaments in the region surrounding the cluster, or the accretion of gas from a smaller filament towards a larger one, is necessary to gain a broader understanding of the full complexity of the kinematics involved in the formation of stellar clusters. Additionally, a study utilising denser molecular tracers, such as NH_3, could be conducted to compare their structures and behaviours near clusters. Also, the infall velocity and the mass accretion rate could be computed to gain a quantitative knowledge.

Acknowledgments

I would like to express my gratitude to Dra. Gemma Busquet for her advice, guidance and unwavering support throughout the course of my project. Also, I would like to thank my family and friends for their patience and encouragement.

[1] P. Myers (2009) "Filamentary Structure of Star-Forming Complexes". The Astrophysical Journal **700**: 1609-1625 (2009).
[2] A. Hacar et al. "Initial Conditions for Star Formation: A Physical Description of the Filamentary ISM". Protostars and Planets VII (2022).
[3] H. Chen et al. "Filamentary Accreation Flows in the Infrared Dark Cloud C14.225-0.506 Revealed by ALMA". The Astrophysical Journal **875**, 24 (2019).
[4] C. Zucker et al. "A Compendium of Distances to Molecular Clouds in the Star Formation Handbook". Astronomy & Astrophysics **633**, A51 (2020).
[5] *Gaia* Collaboration et al. "*Gaia* Data Release 2. Summary of the contents and survey properties". Astronomy & Astrophysics **616**, A1 (2018).
[6] E. Díaz-Márquez et al. "Radio Survey of the Stellar Population in the Infrared Dark Cloud G14.225-0,506". Astronomy & Astrophysics **682**, A180 (2024).
[7] G. Busquet et al. "What is Controlling the Fragmentation in the Infrared Dark Cloud G14.225-0.506?: Different Levels of Fragmentation in Twin Hubs". The Astrophysical Journal **819**, 139 (2016).
[8] S. Ohashi et al. "Dense Core Properties in the Infrared Dark Cloud G14.225-0.506 Revealed by ALMA". The Astrophysical Journal **833**, 209 (2016).
[9] "Atacama Large Millimeter/submillimeter Array". `https://www.almaobservatory.org/en/home/`
[10] "The Cologne Database for Molecular Spectroscopy (CDMS)". `https://cdms.astro.uni-koeln.de`
[11] G. Busquet et al. "Unveiling a Network of Parallel Filaments in the Infrared Dark Cloud G14.225-0.506". The Astrophysical Letters **764**, L26 (2013).
[12] A. Hacar et al. "Opacity Broadening and Interpretation of Suprathermal CO linewidths: Macroscopic Turbulene and Tangles Molecular Clouds". Astronomy & Astrophysics manuscript **591**, 104 (2016).
[13] "Common Astronomy Software Applications (CASA)". `https://casa.nrao.edu/`
[14] E. W. Rosolowsky et al. "Structural Analysis of Molecular Clouds: Dendrograms". The Astrophysical Journal **679**, 1338 (2008).
[15] "Astronomical Dendrograms in Python (`astrodendro`)". `https://dendrograms.readthedocs.io/en/stable/`

V. APPENDIX

FIG. 5: Representation of the countors (left) and dendrograms (right) of the substructures of each of the 20 most relevant structures highlighted in FIG. 2.

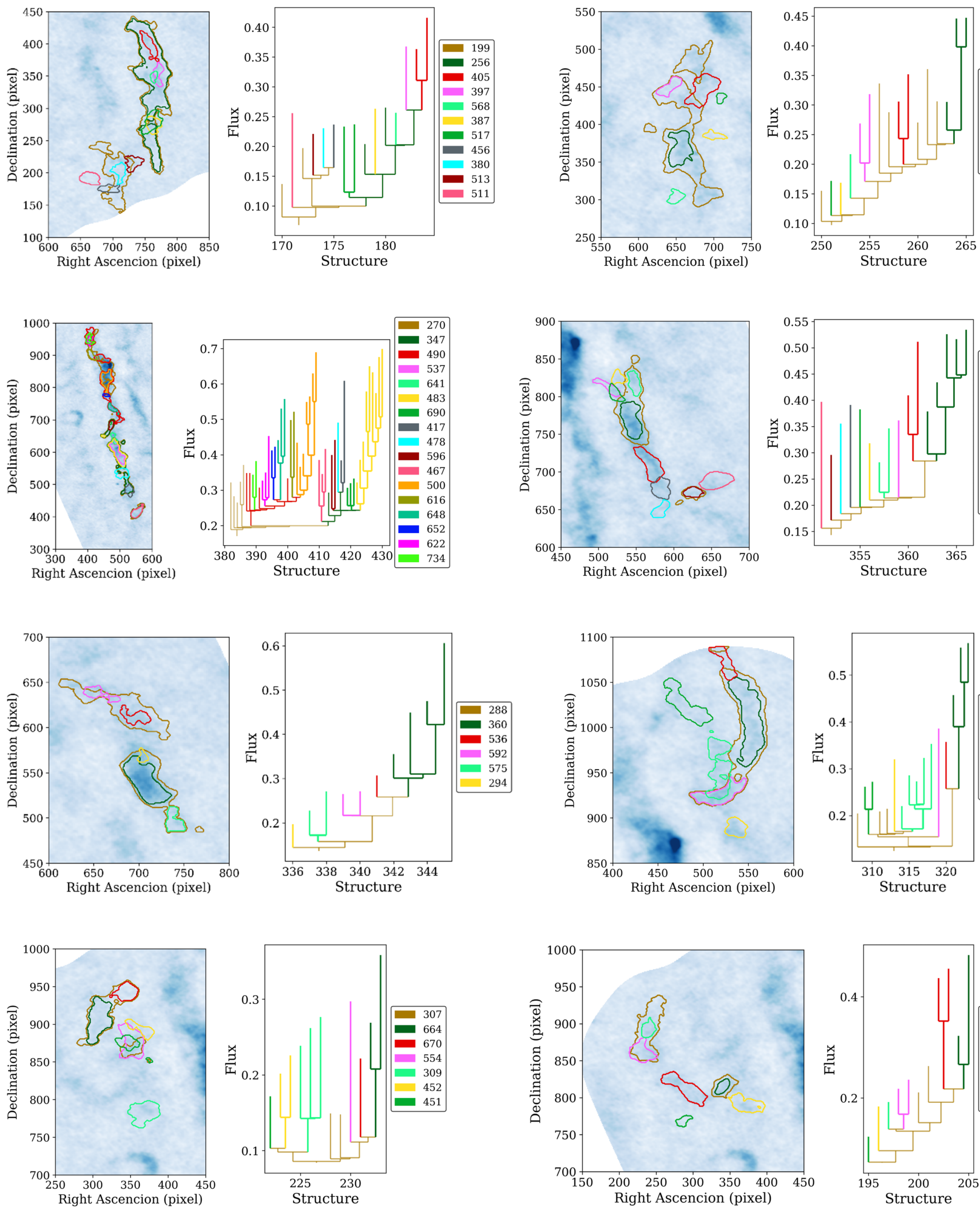

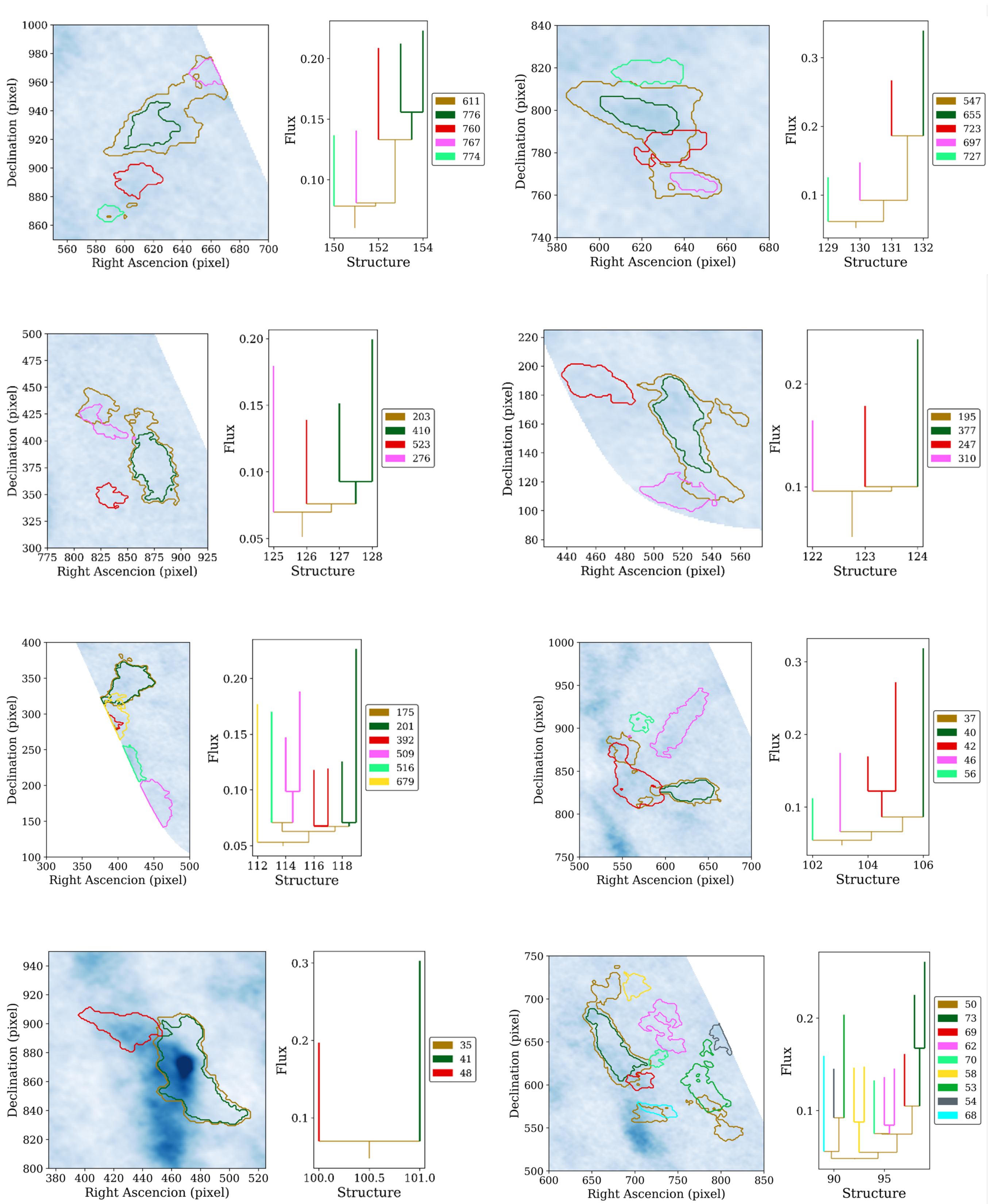
Declination (pixel)
Right Ascencion (pixel)
Flux
Structure
611
776
760
767
774
547
655
723
697
727
203
410
523
276
195
377
247
310
175
201
392
509
516
679
37
40
42
46
56
35
41
48
50
73
69
62
70
58
53
54
68

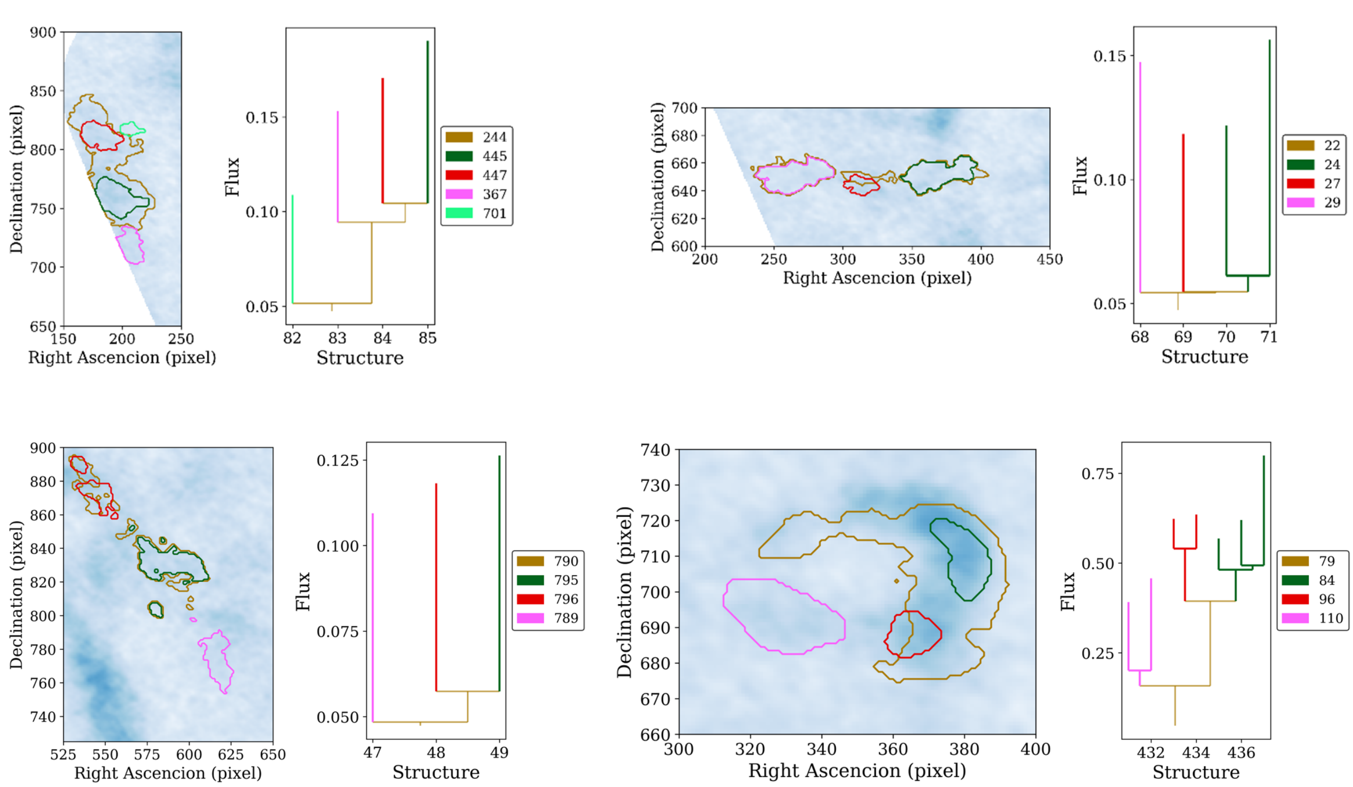
Declination (pixel)
Right Ascencion (pixel)
Flux
Structure
244
445
447
367
701
22
24
27
29
790
795
796
789
79
84
96
110